Materials and Structures
DOI 10.1617/s11527-006-9145-5

ORIGINAL ARTICLE

Cracking, damage and fracture in four dimensions

E. N. Landis · T. Zhang · E. N. Nagy · G. Nagy · W. R. Franklin

Received: 31 March 2005 / Accepted: 26 October 2005

Abstract Concrete and cracking are nearly synonymous despite our best efforts and intentions. Relationships between cracking and the stress states that lead to cracking can be instructive. In an effort to better understand these relationships, X-ray microtomography was used to make high-resolution three-dimensional digital images of small concrete specimens under load. Using 3D image analysis, quantitative measurements of internal crack growth were made that include effects of crack tortuosity, branching and microcracking. Successive images at different levels of cracking and damage provide us with a detailed picture of internal crack progression. When coupled with load-deformation response, bulk material properties such as fracture toughness or damage variables can be quantitatively linked with cracking. Measurements to date have shown distinct fracture regimes linked to crack formation and propagation. In addition, the crack measurements offer a way to provide a physical basis for a scalar damage variable.

Keywords Concrete · Fracture · Damage · Tomography

E. N. Landis (✉) · E. N. Nagy
University of Maine, Orono, USA
e-mail: landis@maine.edu

T. Zhang · G. Nagy · W. R. Franklin
Rensselaer Polytechnic Institute, Troy, USA

1 Introduction

The role of cracks and flaws in materials has been central to our understanding of strength and failure in materials for nearly a century. Since the work of Griffith and the subsequent birth of fracture mechanics, cracks have been the focus of our strength and damage theories. Continuum damage theory further established the role of distributed crack systems on bulk stiffness degradation. Over the past 30 years this body of knowledge has been applied with great enthusiasm to problems of strength, toughness, durability, and overall performance of concrete and reinforced concrete systems. A problem, however, is that despite the substantial efforts of researchers around the world, surprisingly little progress has been made in truly quantitative relationships between crack parameters and bulk material parameters. Indeed, few if any fracture mechanics principles have made their way into building codes or standard design procedures, and after 30 years there is still no standard test to measure fracture toughness!

The theme of the work described in this paper, is that the problems just described ultimately may stem from a fundamental lack of understanding of crack systems in an extremely heterogeneous medium such as concrete. For years we have been thinking and modeling in terms of elliptical cracks, penny-shaped cracks, wing cracks, crack

normal vectors, crack shielding, fictitious cracks, fracture process zones, and so forth. While these concepts and idealizations are most certainly grounded in real phenomena, perhaps the direct application to a complex system such as concrete is too great a stretch.

Thus, in order to help improve our understanding of the complex cracking that occurs in concrete, we are employing high resolution 3D scanning coupled with quantitative 3D image analysis techniques. The goal is to characterize these crack systems in such a way that our dependence on simple geometric forms is minimized. Once this is done, we can make steps to relate crack parameters to bulk material properties. The implied assumption here is that improvements in our understanding of the physical processes involved in damage and fracture will lead to improvements in our ability to predict material performance.

2 Experimental methods

The 3D scanning technique employed here is called X-ray microtomography [1]. It is similar in practice to computed axial tomography (CAT-scans) used in medical imaging in that a sequence of radiographic images made at different angles are mathematically reconstructed to produce a 3D map of an object's X-ray absorption, which in turn can be used to deduce the internal structure of the object. The difference is that microtomography uses extremely high intensity radiation from a synchrotron source. The synchrotron provides a collimated beam, high flux, and narrow bandwidth X-rays. When combined with an appropriate scintillator and digital image capturing system, 3D images with a spatial resolution approaching 1 micron are possible. Because of the synchrotron source, the images have very good dynamic range, and thus subtle variations in material structure can be detected. A schematic diagram of the microtomography system components is presented in Fig. 1. The rotation stage allows imaging of the specimen at different angles, while the microscope objective allows scans of variable magnification.

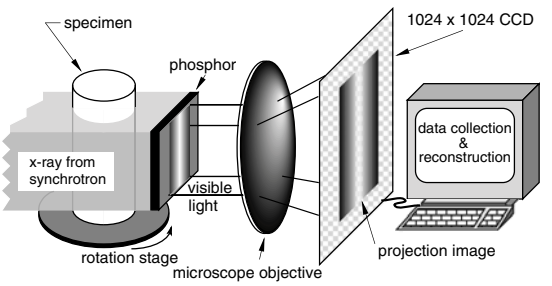

Fig. 1 Illustration of microtomographic scanning set-up

When applied to problems of concrete microstructure, microtomography provides a nice complement to our imaging toolbox. As such it has been used to image cement and concrete in a number of applications, including sulfate attack [2, 3], porosity and pore structure, [4], and fracture [5, 6]. While not as high resolution as electron microscopy, it does offer the advantage of providing true 3D data. Because it is nondestructive, microtomography can be used to scan the same specimen multiple times, allowing us to explore microstructural changes resulting from a number of different agents. This aspect was exploited in the research detailed below.

An example cross sectional "slice" image of concrete microstructure is shown in Fig. 2. In the figure one can see many of the important features of hydrated cement paste: unreacted cement grains (white flecks), pore space (dark spots), transition zones around aggregates, as well as a variable density within an aggregate particle. It

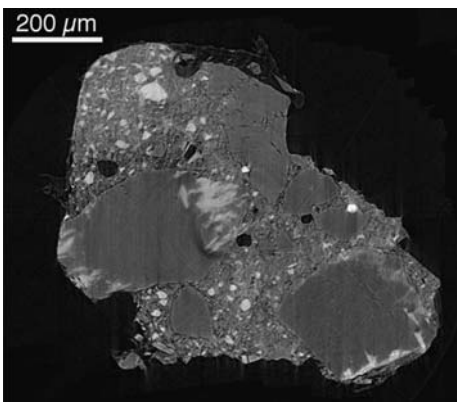

Fig. 2 Example 2D "slice" image taken from 3D tomographic reconstruction

should be emphasized that this is one slice out of the hundreds that are produced in a single scan.

2.1 In situ loading

As previously indicated, the technique was previously utilized in a study of concrete fracture mechanics [5, 6]. For that study, a small compression testing frame was constructed so that tomographic scanning could take place while the specimen was under load. Thus, the same specimen could be scanned multiple times at progressively higher levels of damage. The frame was able to measure applied force and the resulting displacement while being nominally transparent to X-rays. It is illustrated in Fig. 3. The data presented in this paper resulted from those fracture studies.

The microtomographic scanning/loading protocol was as follows. An initial scan of an undamaged specimen was made prior to loading. Then the specimen was loaded to a prescribed deformation, and a subsequent scan was made. The specimen was then unloaded and reloaded for additional scans. This procedure was repeated for at least 4 cycles as illustrated in Fig. 4.

Figure 5 shows a sequence of images taken of a specimen loaded to different levels of damage. In this case the planes shown are perpendicular to the axis of loading. The sequence shows roughly the same plane in each of the scans. (Note that it is not possible to precisely match planes due to nonuniform deformation in the specimen.) The growth of crack networks is clearly shown. In

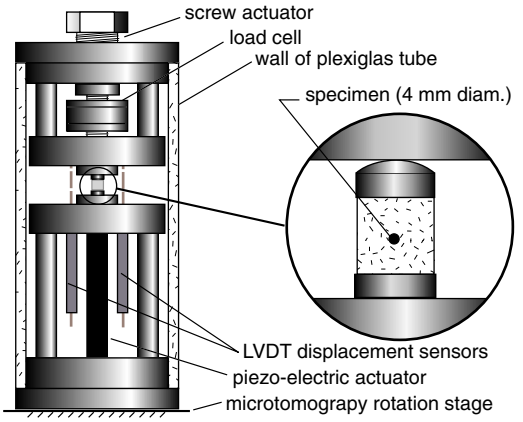

Fig. 3 In situ loading frame

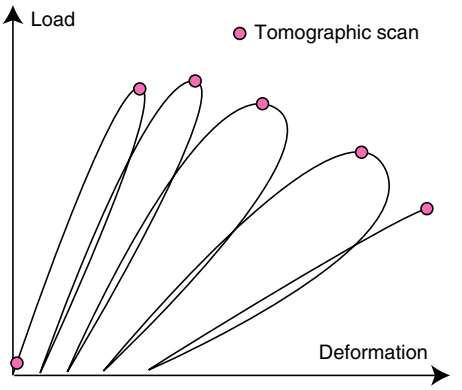

Fig. 4 Load cycles and scanning

subsequent images cracks grow longer, branch, and interconnect as the network extends. It is important to note the complexity of the network. Indeed, we must dispense with some of our traditional simplifications as it would be difficult to characterize such a crack network in terms of conventional plane geometry.

The specimens prepared for this study were small cylinders 4 mm in diameter by 4 mm in height. The small size was required by the constraints of the synchrotron beamline. However, the small specimen size led to a relatively high spatial resolution of 6 microns per voxel. The mix proportion of the specimens was (by mass) 1 part type I portland cement to 2 parts sand to 0.6 parts water. The maximum aggregate size was 0.425 mm. No air entraining or other admixtures were used.

3 3D Image processing

As the data produced by the tomographic scans is digital, we have at our disposal an extensive library of image analysis and image processing techniques. In the work described here, a variety of 3D analysis routines were developed in order to extract quantitative measurements from the acquired data. Specifically, we utilized routines to (1) segment images to separate void space from solid, (2) isolate the specimen, (3) isolate void objects, and (4) measure properties of void objects and displacement fields. Two different approaches were used to isolate crack objects, as is detailed below.

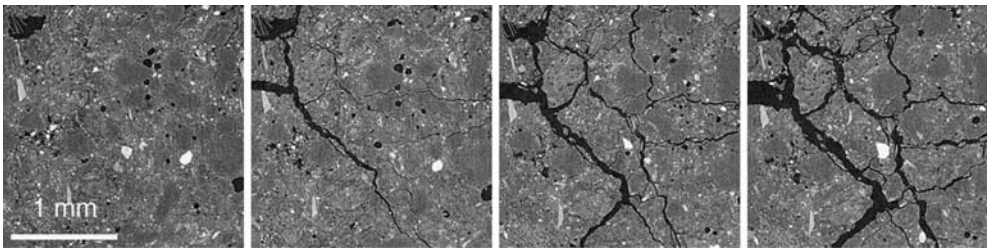

Fig. 5 Images of specimen segment at different levels of damage

3.1 Image segmentation

Microtomography produces images where the voxel (3D pixel) intensity is roughly proportional to the density of the material at that point. A histogram of voxel intensities of a porous material such as concrete shows distinct peaks at intensities representing the solid material and the void space. As such, a simple way to separate the two is to establish a threshold intensity at the minimum between the two peaks [7]. Any voxel with an intensity above the threshold is considered solid, and is made white, while any voxel with an intensity below the threshold is considered void, and is colored black. Figure 6 illustrates the effect applied to the image segments of Fig. 5. As can be seen in the images, void and crack space are clearly visible.

3.2 Specimen isolation

Because the specimens used in this work were of an irregular shape, it became necessary to develop a routine to isolate the specimen from the surrounding background. In doing this, all subsequent image analysis could be focused exclusively on the specimen interior, rather than the entire field of view.

Two steps were used to separate interior void space from exterior space. First, a shrink wrapping algorithm [8] was used to define the boundary of the specimen, as illustrated in Fig. 7. The ''wrapper'' encloses the boundary of the specimen while preserving all the irregularities on the boundary. Second, the result of the shrink wrapping was combined with the previously determined binary image to separate the internal void

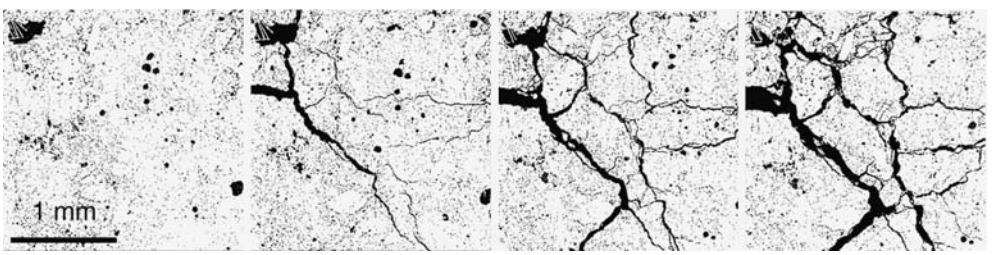

Fig. 6 Black and white images where black indicates void space, white indicates solid

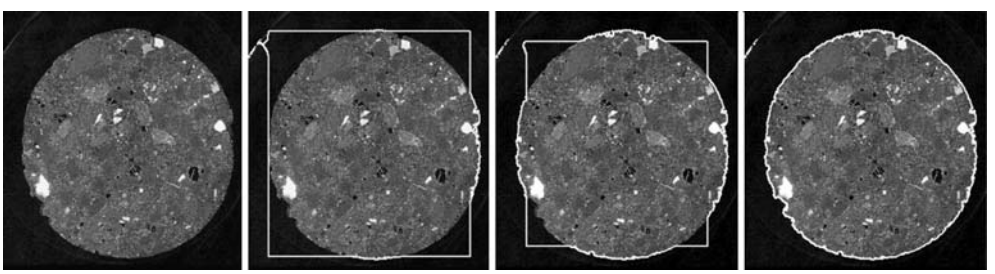

Fig. 7 Application of shrinkwrap algorithm to isolate specimen from background

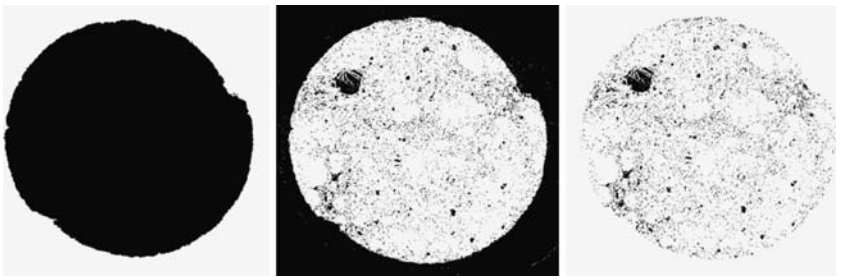

Fig. 8 Logical 'AND' applied to two leftmost images. Any pixel that is black in both images becomes black in the resulting (right-hand) image

objects. As illustrated in Fig. 8, a logical 'AND' is applied to two images. The output from the shrink wrap is shown on the left as a solid object. Any voxel that is black in both the left image and the center black & white image remains black in the right-hand image. The result is an image that includes only the internal void space. Thus, any subsequent analysis of void objects applies only to the internal objects. The use of a logical statement is much more computationally efficient than image coordinate arithmetic.

3.3 Object connectivity

In order to make measurements of different object properties, each individual void object must first be isolated and labeled. This is done by evaluating the connectivity of the black voxels. If two adjacent black objects share a face (6-connectivity), edge (18-connectivity), or corner (26-connectivity) they are considered as part of the same object. In this work, a fast, robust 3D connected components algorithm developed by Franklin [9] was used. This program returns (among other image statistics) the number of discrete objects, and the volume and surface area of each object. Volume is determined by the number of voxels in the object, while surface area is determined by the number of free voxel faces. (That is, black voxel faces that are in contact with white voxels.)

Table 1 Measurements of void/crack system

Scan	Total number of void objects	Total volume of void objects $(mm)^3$	Totals surface area of void objects $(mm)^3$
1	3.12×10^6	2.56	554
2	3.06×10^6	3.36	595
3	3.09×10^6	4.17	680
4	2.17×10^6	5.94	716
5	2.54×10^6	6.86	733

4 Crack measurements

The measurements resulting from the connected components analysis is enlightening. Table 1 shows the measurement results from five different scans of the same specimen at successively higher levels of deformation. Even in the undamaged specimen (scan 1) there are over 3 million void objects in a 4 mm diameter by 4 mm high cylinder. A majority of these are very small objects of 1 to 3 voxels (216–648 μm^3) in volume. The total volume of the void space in the first scan corresponds to a porosity of roughly 5%, which is reasonable for the level of resolution in the scans. The higher levels of porosity typically measured using techniques such as mercury intrusion porosimetry result from a much finer resolution.

Of particular interest in this work are the changes in void object measurements that occur as the specimen becomes progressively more damaged. For simplicity, any growth in cumulative object volume or surface area above that measured in the first (undamaged specimen) scan is hereafter referred to as cracks. The first item to note is that the total number of void objects actually *decreases* with progressive damage. While this is perhaps not intuitive, we must recognize that during damage growth many initially isolated void spaces become connected by the resulting cracks. Thus, void volume and surface area can increase while number of void objects decreases.

The relationship between the growth in volume and the growth in surface area provides additional insight. Initially, increases in both crack surface area and volume are significant, as judged by the

relative increases seen in scans 2 and 3 in Table 1. This would be indicative of significant crack extension along with a corresponding crack opening. In the later stages of damage however, the incremental increases in surface area are relatively small, while the increases in volume are still significant. This is best illustrated in scan 4, where there is a 42% increase in crack volume corresponding to only a 5% increase in crack surface area. Clearly significant crack opening is taking place. This phenomenon likely explains the mobilization of fracture toughening mechanisms as discussed below.

5 Connections with bulk properties

The above measurements are particularly useful when used in conjunction with changes in bulk material properties. In work done to date, crack data has been used to calculate fracture energy [5, 6], and has been used in conjunction with changes in specimen compliance to relate crack properties to a scalar damage variable [10]. In both cases, crack properties are related to properties of the specimen load-deformation response. Relevant load-deformation properties are shown in Table 2.

5.1 Fracture energy

The first chapter of any fracture mechanics textbook defines fracture energy in terms of the conversion of available strain energy to new crack surfaces. That is:

$$G_i = \frac{\mathrm{d}U_i}{\mathrm{d}A_i} \tag{1}$$

where G_i is the incremental energy required to grow a crack by an area of $\mathrm{d}A_i$. $\mathrm{d}U_i$ is the incremental change in strain energy. Thus one simply needs to measure the change in strain energy that accompanies an incremental growth in crack area. In the fracture mechanics text books, this relationship is traditionally followed by examples where the fracture energy can be calculated for idealized geometries: planer cracks in through-thickness 2D systems.

In this work, however, no geometric assumptions need be made. Changes in strain energy can be calculated using available load-deformation data. This can then be related to the corresponding change in crack surface area to produce the incremental fracture energy using Eq. (1). The cumulative net change in strain energy is plotted against the net increase in crack surface area for the specimen data presented in Table 2, along with that from a second specimen, in Fig. 9. The plot shows two clear fracture regimes: an initial linear section with a slope of about 90 J/mm^2, and a second linear regime with a slope approaching 400 J/

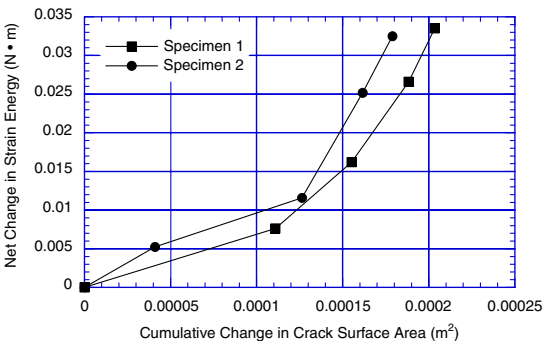

Fig. 9 Plot of cumulative change in strain energy versus crack surface energy

Table 2 Changes in specimen and crack properties from initial condition

Scan	Specimen elastic modulus (GPa)	Net Change in Strain Energy(J)	Damage Variable,D	Net increase in crack object volume (mm)^3	Net increase in crack object surface area(mm)^3
1	20.7	0	0	–	–
2	20.5	0.0052	9.7×10^{-3}	0.80	41
3	16.2	0.0115	0.22	1.61	126
4	9.73	0.0251	0.53	3.38	162
5	6.63	0.0324	0.68	4.30	179

mm^2. We have suggested that the initial segment represents fracture dominated by simple tensile cracking, while the latter segment represents the mobilization of a variety of toughening mechanisms, including friction, crack bridging and interlocking [6].

It is important to note that no assumptions about crack geometry were made in the above fracture energy calculation.

5.2 Scalar damage variable

Continuum damage mechanics is an elegant way to handle the gradual degradation in material properties due to diffuse cracking and void growth. However, in the usual approach, crack distributions are assumed to have a simplified geometry. The relationship between cracking and the resulting material stiffness degradation is based on either micromechanics-based arguments, or continuum representations of crack densities. In either case the relationships tend to ultimately boil down to averaging constants that may or may not have any physical reality.

In an effort to give a physical basis to a scalar damage variable, without making assumptions about the geometries of crack distributions, measured changes in specimen stiffness were related to changes in crack properties. The damage variable, D_i, was calculated from the changes in specimens stiffness as follows:

$$E_i = E_1(1 - D_i) \tag{2}$$

where E_1 is the initial (undamaged) elastic modulus, and E_i is the subsequent (damaged) modulus. D_i was calculated by rearranging Eq. (2), and is presented in Table 2. D is plotted against the cumulative increase in crack surface area in Fig. 10, while Fig. 11 shows D plotted against crack volume.

Upon first glance these two plotted relationships might seem counter intuitive. Clearly there is known energy dissipation associated with crack growth that should in turn affect specimen compliance. It is likely however, that the apparent nonlinear relationship shown in Fig. 10 stems from the fact that the measured cracks have a wide, but not random, range of orientations,

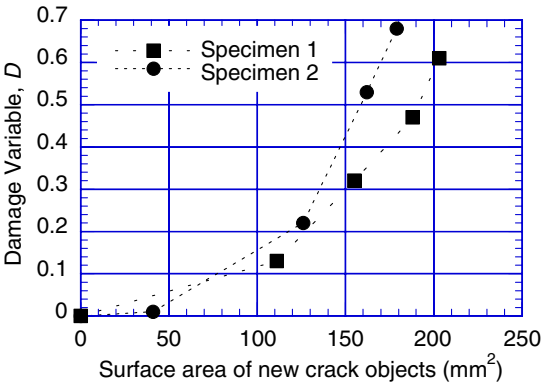

Fig. 10 Damage variable plotted against cumulative increase in crack object surface area

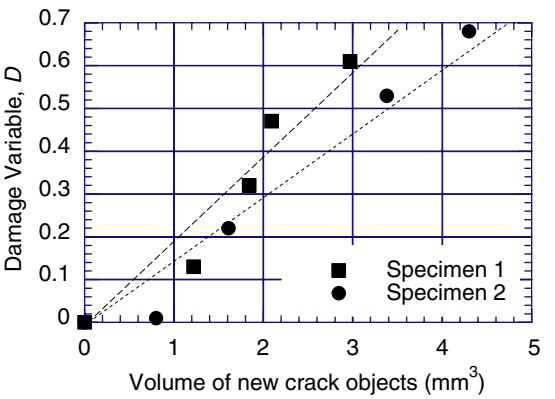

Fig. 11 Damage variable plotted against cumulative increase in crack object volume

which might necessitate the need for a higher order anisotropic damage representation. A tensorial representation of the microstructure presented here might be challenging, as single crack objects are themselves multi-faceted and not amenable to traditional geometric descriptors such as crack normal vectors. The crack volume basis for a damage descriptor, while perhaps less appealing from first principles, offers several advantages. First, a reasonably linear relationship as shown here is always desirable for simplicity. Second, the prospects for an in situ measurement of crack volume, while still not currently reliable, are at least foreseeable in that crack volume can be tied to porosity and pore size distribution, which may one day be readily measurable with techniques such as ultrasonic or electromagnetic imaging.

6 Conclusions

The work presented in this paper represents a small, but deliberate first step in an attempt to wean ourselves from simple geometric descriptors of cracks and crack systems. Simple characterizations of 3D surface areas and volumes are a logical starting point, and indeed they provide useful insight into damage evolution in a relatively simple loading regime. The necessary next steps will be to develop more sophisticated descriptors of the crack systems: descriptors that can adequately represent the complexity and interconnectivity of the systems. Once these descriptors are developed, they may be used in material models that are based on a realistic physical picture of microstructure and all the associated mechanisms that affect material behavior.

References

1. Flannery BP, Deckman HW, Roberge WG, D'Amico KL (1987) Three-dimensional X-ray microtomography. Science 237:1439–1444
2. Bentz DP, Martys NS, Stutzman PE, Levenson MS, Garboczi EJ, Dunsmuir J, Schwartz LM (1995) X-ray microtomography of an ASTM C109 mortar exposed to sulfate attack. In: Diamond S (ed) Microstructure of cement-based systems/bonding and interfaces in cementitious materials. Materials Research Society, Pittsburgh
3. Stock SR, Naik NK, Wilkinson AP, Kurtis KE (2002) X-ray microtomography (microCT) of the progression of sulfate attack of cement paste. Cement Concrete Res 32(10):1673–1675
4. Bentz DP, Quenard DA, Kunzel HM, Baruchel J, Peyrin F, Martys NS, Garboczi EJ (2000) Microstructure and transport properties of porous building materials II: three-dimensional X-ray tomographic studies. Mater Struct 33:147–153
5. Landis EN, Nagy EN, Keane DT, Nagy G (1999) A technique to measure three-dimensional work-of-fracture of concrete in compression. J Eng Mech 125(6):599–605
6. Landis EN, Nagy EN, Keane DT (2003) Microstructure and Fracture in Three Dimensions. Eng Fract Mech 70(7):911–925
7. Gonzalez RC, Woods RE (2002) Digital image processing. Prentice Hall, Upper Saddle River
8. Zhang T (2004) Identification of structural changes from volumetric image sequence', PhD Thesis, Computer and Systems Engineering, Rensselaer Polytechnic Institute, Troy, NY, USA
9. Franklin WR (1999) Connect, http://www.ecse.rpi.edu/Homepages/wrf/research/connect/index.html,
10. Landis EN (2006) Towards a physical damage variable for concrete. J Eng Mech 132(7)